11. D. E. Smith *et al.*, *Science* **284**, 1495 (1999).
12. M. H. Carr, *The Surface of Mars* (Yale Univ. Press, New Haven, CT, 1981).
13. H. Frey, S. E. Sakimoto, J. Roark, *Geophys. Res. Lett.* **25**, 4409 (1998).
14. D. E. Wilhelms and S. W. Squyres, *Nature* **309**, 138 (1984); G. E. McGill, *J. Geophys. Res.* **94**, 2753 (1989).
15. H. V. Frey and R. A. Schultz, *Geophys. Res. Lett.* **15**, 229 (1988).
16. S. R. Bratt, S. C. Solomon, J. W. Head, C. H. Thurber, *J. Geophys. Res.* **90**, 3049 (1985); M. T. Zuber, D. E. Smith, F. G. Lemoine, G. A. Neumann, *Science* **266**, 1839 (1994).
17. S. C. Solomon and J. W. Head, *J. Geophys. Res.* **82**, 9755 (1982).
18. W. B. Banerdt, M. P. Golombek, K. L. Tanaka, in *Mars*, H. H. Kieffer, B. M. Jakosky, C. W. Snyder, M. S. Matthews, Eds. (Univ. of Arizona Press, Tucson, AZ, 1992), pp. 249–297.
19. J. Morgan and M. Warner, *Geology* **27**, 407 (1999).
20. F. Sohl and T. Spohn, *J. Geophys. Res.* **102**, 1613 (1997).
21. Using the method of (*47*), we estimated the relaxation time for a degree-1 crustal thickness variation on a self-gravitating spherical planet. We assumed a mechanically strong upper crust of thickness 20 km and a uniform-thickness viscous lower crust. Densities are as in (*8*).
22. G. Schubert and T. Spohn, *J. Geophys. Res.* **95**, 14095 (1990).
23. O. Grasset and E. M. Parmentier, *J. Geophys. Res.* **103**, 18171 (1998); G. Choblet, O. Grasset, E. M. Parmentier, C. Sotin, *Lunar Planet. Sci.* **30**, 1556 (1998); T. Spohn, D. Breuer, V. Conzelmann, *Eos (Fall Suppl.)* **80**, F619 (1999).
24. M. Simons, S. C. Solomon, B. H. Hager, *Geophys. J. Int.* **131**, 24 (1997); F. J. Simons, M. T. Zuber, J. Korenaga, *J. Geophys. Res.*, in press. The admittance is the response function between spectral gravity and topography, and the coherence is the square of the correlation coefficient between normalized spectral amplitudes of gravity and topography. The admittance approach assumes surface loading of an elastic spherical shell, whereas the coherence approach assumes surface and subsurface loading of an elastic plate. Both methods use densities as in (*8*).
25. M. H. Acuña *et al.*, *Science* **284**, 790 (1999).
26. J. E. P. Connerney *et al.*, *Science* **284**, 794 (1999).
27. Common magnetic minerals on Earth carry remanent magnetization only at temperatures less than the Curie temperature of 580° (magnetite) to 680°C (hematite) [D. J. Dunlop and O. Ozdemir, *Rock Magnetism* (Cambridge Univ. Press, Cambridge, 1997)].
28. D. E. Smith *et al.*, *Science* **279**, 1686 (1998).
29. D. W. Forsyth, *J. Geophys. Res.* **90**, 12623 (1985).
30. Given the similar diameters of Hellas and Utopia (*11*), we used the current gravitational and topographic signatures of Hellas and calculated the trade-off between T_e and fill density that is required to explain Utopia. For Hellas, we used a depth of 11 km, a degree-6 (corresponding to the basin diameter) gravity anomaly of −160 mGal, and a crust-mantle boundary as in Fig. 1C. For Utopia, we used a depth of 2.5 km and a gravity anomaly of 270 mGal. We calculated T_e as in (*48*). If the primary contributor to Utopia basin fill is sedimentary (density = 2200 kg m^{-3}), then for a local crustal density comparable to that of shergottites (3200 kg m^{-3}), the same elastic thickness (100 km) is obtained as for volcanic filling of a crust having the density assumed for the model of Fig. 1C.
31. K. L. Tanaka, D. H. Scott, R. Greeley, in (*18*), pp. 345–382.
32. A. B. Watts, J. H. Bodine, M. S. Steckler, *J. Geophys. Res.* **85**, 5369 (1980).
33. S. C. Solomon and J. W. Head, *J. Geophys. Res.* **95**, 11073 (1990); M. K. McNutt, *J. Geophys. Res.* **89**, 11180 (1984). We converted effective elastic thickness (T_e) to heat flow via computation of the mechanical thickness of an elastic-plastic plate (T_{mech}). The approach entails adopting a range of representative strain rates (10^{-19} s^{-1} and 10^{-15} s^{-1}) and ductile flow laws for the lower lithosphere (*49*) and constructing models of bending stress that are consistent with a best-fit lithospheric strength envelope (*50*).
34. D. W. Forsyth, *J. Geophys. Res.* **98**, 16073 (1993).
35. N. H. Sleep, *J. Geophys. Res.* **99**, 5639 (1994).
36. F. Nimmo and D. J. Stevenson, *J. Geophys. Res.*, in press.
37. J. W. Head III *et al.*, *Science* **286**, 2134 (1999).
38. T. J. Parker, D. S. Gorsline, R. S. Saunders, D. C. Pieri, D. M. Schneeberger, *J. Geophys. Res.* **98**, 11061 (1993).
39. The proposed buried channels are situated within the Tharsis negative gravity ring, which is likely a membrane response to Tharsis loading (*51*). The linear anomalies are superposed on the relatively broad membrane gravity signal.
40. I. Klaucke, R. Hesse, W. B. F. Ryan, *Sedimentology* **44**, 1093 (1997); *Geol. Soc. Am. Bull.* **110**, 22 (1998).
41. F. G. Lemoine *et al.*, *Eos (Fall Suppl.)* **80**, F618 (1999); W. L. Sjogren, D. Yuan, A. S. Konopliv, *Eos (Fall Suppl.)* **80**, F618 (1999).
42. F. G. Lemoine *et al.*, in preparation.
43. W. M. Kaula, *Theory of Satellite Geodesy* (Blaisdell, Waltham, MA, 1966).
44. S. S. C. Wu, *USGS Map I-2160* (1991).
45. M. A. Wieczorek and R. J. Phillips, *J. Geophys. Res.* **103**, 1715 (1998).
46. H. Y. McSween Jr., *Rev. Geophys.* **23**, 391 (1985).
47. S. Zhong and M. T. Zuber, *J. Geophys. Res.*, in press.
48. D. L. Turcotte, R. J. Willemann, W. F. Haxby, J. Norberry, *J. Geophys. Res.* **86**, 3951 (1981).
49. C. Goetze, *Philos. Trans. R. Soc. London Ser. A* **288**, 99 (1978); Y. Caristan, *J. Geophys. Res.* **87**, 6781 (1982).
50. W. F. Brace and D. L. Kohlstedt, *J. Geophys. Res.* **85**, 6248 (1980).
51. R. J. Phillips, M. T. Zuber, S. A. Hauck, R. M. Williams, K. B. Portle, *Lunar Planet. Sci.* **31** (abstr. no. 1303) (2000).

52. We thank the MGS spacecraft and mission operations teams at the Jet Propulsion Laboratory and Lockheed-Martin Astronautics for their contributions to this effort. We also acknowledge R. Follas, J. Abshire, and the MOLA Instrument Team for laser performance information; M. Torrence and J. Schott for assistance in altimetry processing; R. Simpson, P. Priest, S. Asmar, and J. Twicken for assistance in tracking data acquisition and processing; S. Fricke for help with orbit determination; M. Wieczorek for compilation of martian meteorite densities; M. Simons and F. Simons (no relation) for codes used in the lithosphere thickness inversions; and D. Stevenson and N. Sleep for helpful reviews. The MGS Radio Science and MOLA investigations are supported by the NASA Mars Exploration Program.

20 January 2000; accepted 18 February 2000

Suppression of Rain and Snow by Urban and Industrial Air Pollution

Daniel Rosenfeld

Direct evidence demonstrates that urban and industrial air pollution can completely shut off precipitation from clouds that have temperatures at their tops of about −10°C over large areas. Satellite data reveal plumes of reduced cloud particle size and suppressed precipitation originating from major urban areas and from industrial facilities such as power plants. Measurements obtained by the Tropical Rainfall Measuring Mission satellite reveal that both cloud droplet coalescence and ice precipitation formation are inhibited in polluted clouds.

The precipitation-forming processes in clouds depend to a large extent on the presence of aerosols, specifically cloud condensation nuclei (CCN) and ice nuclei. The large concentrations of small CCN in the smoke from burning vegetation nucleate many small cloud droplets (*1*, *2*) that coalesce inefficiently into raindrops (*3*, *4*). Although this effect has been suspected for many years (*5*, *6*), conclusive evidence that smoke from burning vegetation suppresses precipitation was obtained recently with the observations of the Tropical Rainfall Measuring Mission (TRMM) (*7*) satellite (*8*).

Much less is known, however, about the impact of aerosols from urban and industrial air pollution on precipitation. It was assumed initially that industrial and urban pollution inhibited precipitation, similar to the smoke from burning vegetation (*9*). Later, reports of enhanced rainfall downwind of paper mills (*10*) and over major urban areas (*11*) suggested that giant CCN enhanced precipitation (*12*), but attempts to correlate the urban-enhanced rainfall to the air pollution sources failed to show any relation (*13*). Another explanation for the urban rain enhancement invoked the heat-island effect and increased friction, both of which would tend to increase the surface convergence, resulting in more cloud growth and rainfall over and downwind of the urban areas (*14*). Furthermore, the recent suggestion (*15*) that air pollution might enhance precipitation on a large scale in northeastern America and the accompanying speculative explanations demonstrate how little is known about the subject.

Space-borne (*16*) and in situ aircraft (*17*) measurements of ship tracks in marine stratocumulus clouds provided the first evidence that effluents from ship stacks change cloud microstructure by redistributing their water into a larger number of smaller droplets. Albrecht (*18*) suggested that the drizzle, which normally occurs in marine stratocumulus clouds in clean air, would be inhibited from the clouds with reduced droplet size,

Institute of Earth Sciences, The Hebrew University of Jerusalem, Givat Ram, Jerusalem, Israel. E-mail: daniel@vms.huji.ac.il

thereby increasing the cloud water content and longevity. Extrapolation to clouds that are sufficiently thick for raining (i.e., at least 2 km from base to top) would mean that the effluents have the potential to suppress precipitation over ocean and over land. However, pollution tracks in any clouds over land were not reported in previous studies. Application of the imaging scheme of Rosenfeld and Lensky (*6*) to the Advanced Very High Resolution Radiometer (AVHRR) on board the National Oceanic and Atmospheric Administration (NOAA) orbiting weather satellites revealed numerous ship track–like features in clouds over land, created by major urban and industrial pollution sources. Illustrations of such tracks from Turkey (Fig. 1A), Canada (Fig. 1B), and Australia (Fig. 1C) are shown. Because the tracks clearly originate from pollution sources, they will be called hereafter "pollution tracks."

The pollution tracks in Turkey (Fig. 1A) originate from several sources in and near the cities of Istanbul, Izmit, and Bursa.

The pollution track in Canada (Fig. 1B) originates from Flin-Flon, Manitoba, the home of the Hudson Bay Mining and Smelting Company. That location has been a frequent source for such tracks. Other sources in Canada have been observed, but not reported here.

Study of the pollution tracks emanating from the region of Adelaide, South Australia, Australia, is especially interesting. They received special attention because of their intensity and frequent occurrence. These pollution tracks were identified in the clouds of all 47 AVHRR images on different days examined in which stratocumulus and cumulus clouds with tops warmer than about −12°C existed over the region. The pollution tracks in Fig. 1C coincide with the following major industrial and urban areas: (i) Port Augusta has a 520-MW power plant operating on brown coal, providing electricity to the nearby mines and to the adjacent large steel industry in Whyalla. (ii) Port Pirie is the home of the world's largest lead smelter and refinery. (iii) Adelaide has industry for processing minerals mined in the vicinity. Among these are Australia's largest cement plant, located on the Port Adelaide River. A major oil refinery and a power plant are located 20 km to the south of the city near the origin of the strongest pollution track in Fig. 1C.

The 1998–99 annual average of effluents from the stack of Port Augusta power plant, which is equipped with an electrostatic precipitator, was 43 kg hour^{-1} of submicrometer ash particles with modal diameter of 0.14 μm. The gaseous annual average of effluents for the same time period is 1108 kg hour^{-1} of SO_2 and 1655 kg hour^{-1} of NO_x (*19*). Apparently, part of the ash particles act as CCN at short range, and chemical reactions of the gases produce additional CCN hundreds of kilometers farther downwind from the pollution source, mainly in the form of sulfates.

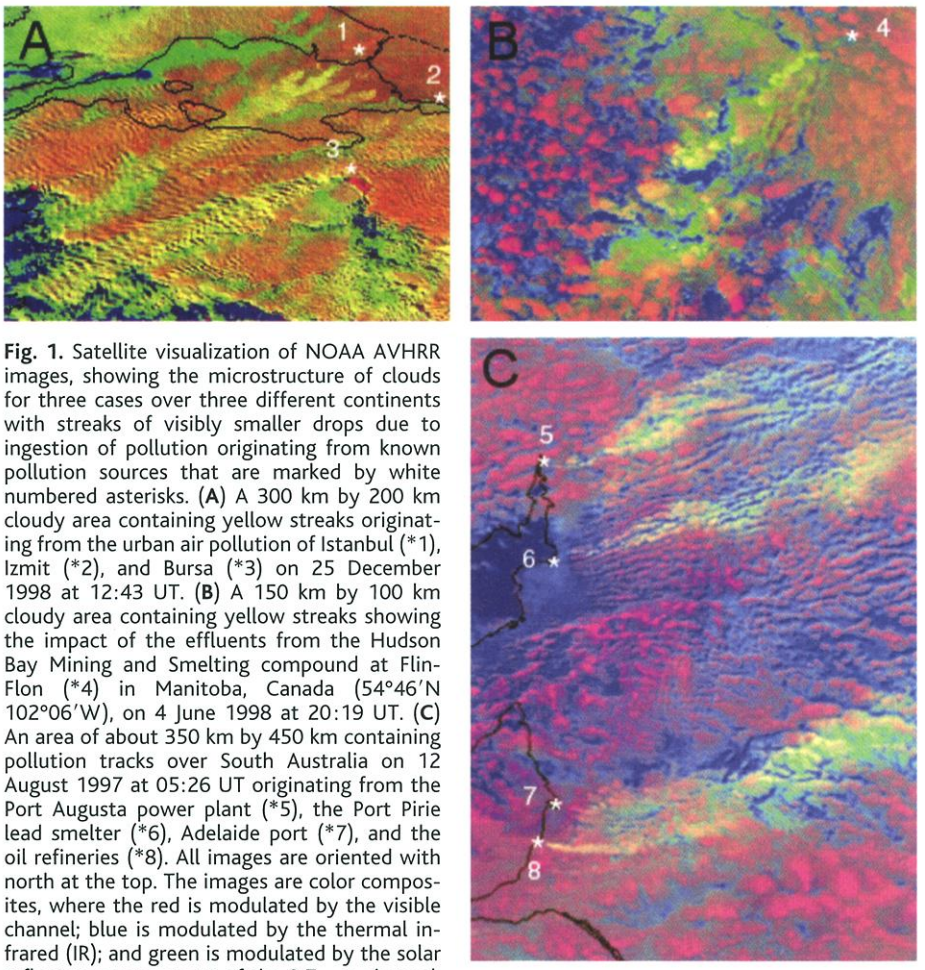

Fig. 1. Satellite visualization of NOAA AVHRR images, showing the microstructure of clouds for three cases over three different continents with streaks of visibly smaller drops due to ingestion of pollution originating from known pollution sources that are marked by white numbered asterisks. (**A**) A 300 km by 200 km cloudy area containing yellow streaks originating from the urban air pollution of Istanbul (*1), Izmit (*2), and Bursa (*3) on 25 December 1998 at 12:43 UT. (**B**) A 150 km by 100 km cloudy area containing yellow streaks showing the impact of the effluents from the Hudson Bay Mining and Smelting compound at Flin-Flon (*4) in Manitoba, Canada (54°46′N 102°06′W), on 4 June 1998 at 20:19 UT. (**C**) An area of about 350 km by 450 km containing pollution tracks over South Australia on 12 August 1997 at 05:26 UT originating from the Port Augusta power plant (*5), the Port Pirie lead smelter (*6), Adelaide port (*7), and the oil refineries (*8). All images are oriented with north at the top. The images are color composites, where the red is modulated by the visible channel; blue is modulated by the thermal infrared (IR); and green is modulated by the solar reflectance component of the 3.7-μm channel, where larger (greener) reflectance indicates smaller droplets. The composition of the channels determines the color of the clouds, where red represents clouds with large drops and yellow represents clouds with small drops. The blue background represents the ground surface below the clouds. A full description of the color palettes and their meaning is provided by Rosenfeld and Lensky (*6*).

The AVHRR data were used to retrieve the dependence of the indicated effective radius $r_e = \langle r^3 \rangle / \langle r^2 \rangle$, where r is the radius of the cloud droplets in the measurement volume, on cloud temperature T. The method of Rosenfeld and Lensky (*6*) was used to derive the T-r_e relations for inference of the precipitation-forming processes in the clouds.

The median r_e of the cloud tops in the pollution plumes (Figs. 1 through 3) was considerably less than the precipitation threshold of 14 μm (*20*). Outside the plumes, however, r_e increased steeply with decreasing T to more than 25 μm, indicating that the cloud droplets in the general area were coalescing into precipitation. At the same time, little growth of r_e with decreasing T was indicated within the pollution plumes, indicating a lack of coalescence and, thus, suppressed precipitation.

These inferences are validated using the additional sensors onboard the TRMM satellite. The TRMM instruments used here are the visible and infrared sensor (VIRS), the precipitation radar (PR), and the TRMM passive microwave imager (TMI). The VIRS is similar to the NOAA AVHRR, but it uses a 2-km subsatellite resolution instead of the 1.1-km resolution used by the AVHRR to obtain the T-r_e relations. PR is a 2.2-cm radar with a subsatellite resolution of 250 m vertically by 4 km horizontally. The minimum detectable signal is about 17 dBZ [decibel of Z (mm^{6}m^{-3})], which is equivalent to about 0.7 mm hour^{-1}. The PR is used to measure the precipitation that forms in the clouds. The TMI uses a 85-GHz vertical polarization brightness temperature (T_{85}) to detect the water in nonprecipitating clouds.

The TRMM measurements are validated by an extensive ground validation program (*21*). Preliminary results show variability of about 25% between rain gauges and TRMM rainfall over large areas, with some TRMM underestimation with the heavier rainfall (*22*). The simultaneous spaceborne measurements of

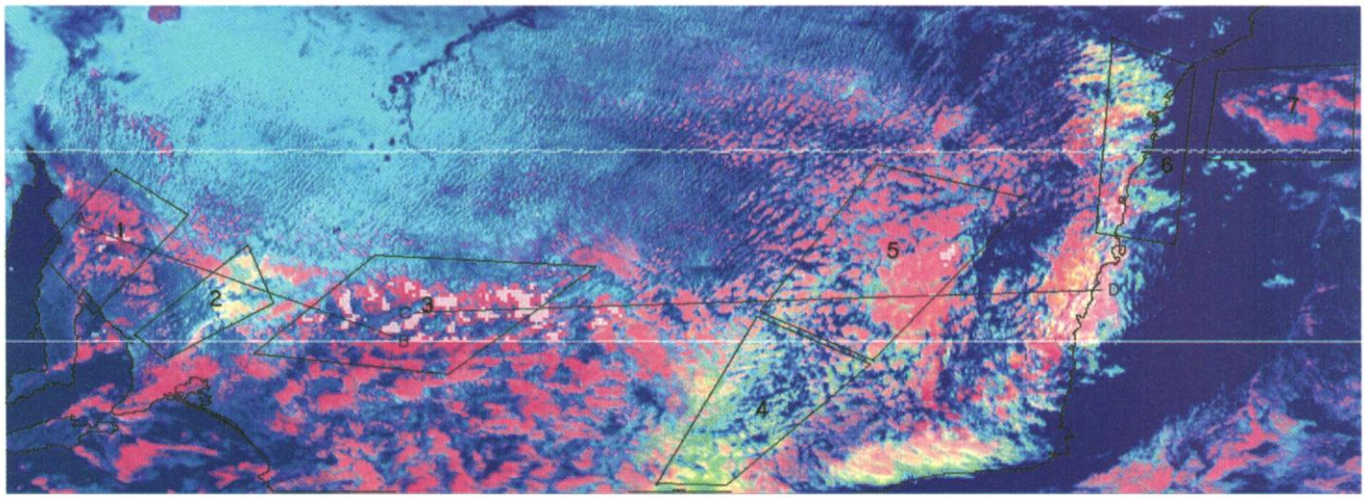

Fig. 2. Satellite visualization of the TRMM VIRS, with the precipitation information in the white overlay. The white patches denote precipitation echoes as observed by the TRMM PR. The two parallel lines delimit the 230-km PR swath. The swath is oriented from west to east (left to right, respectively). The image shows pollution plumes in the clouds over southeastern Australia on 21 October 1998 at 04:44 UT. The lines AB and CD show the locations of the vertical cross sections presented in Fig. 5.

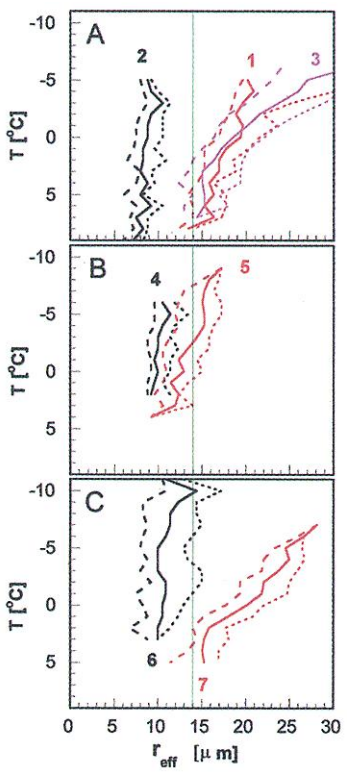

Fig. 3. Analysis of the T-r_e relations, where T is the temperature and r_e (r_{eff}) is the cloud particle effective radius for the clouds in the seven boxes (traces numbered 1 through 7) in Fig. 2. Plotted are the 15th (long dashed line), 50th (solid line), and 85th (short dashed line) percentiles of r_e for each 1°C interval. The black lines correspond to the boxed areas of pollution. The vertical green line marks the 14-μm precipitation threshold. A full description of the T-r_e charts and their meaning is provided by Rosenfeld and Lensky (*6*).

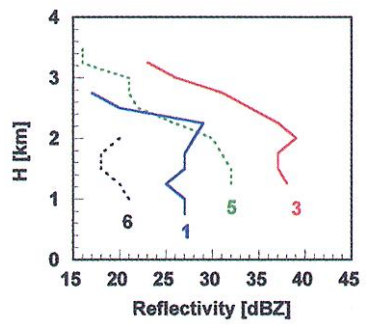

Fig. 4. Vertical profiles of the precipitation echo intensities as measured by the TRMM PR for the various boxes in Fig. 2. The peak near 2 km corresponds to enhanced echoes from snowmelt just below the 0°C isotherm. Box 2 had no detectable precipitation. Boxes 4 and 7 are outside the radar swath. H, cloud height.

cloud microphysics (VIRS), cloud water (TMI), and precipitation (PR) make it possible to relate the precipitation to cloud microstructure.

The TRMM overpass selected for analysis here is from 21 October 1998 at 04:41 UT, a time of strong pollution-track signatures in the clouds throughout southeastern Australia (Fig. 2). Seven boxes within the image were delimited for analyses of the dependence of r_e (Fig. 3) and the PR reflectivities (Fig. 4) as a function of T. Box 2 encloses a pollution plume that is clearly visible by the yellow coloring, which indicates the small r_e of the cloud particles downwind of Adelaide. According to the T-r_e relations presented in Fig. 3A, the clouds in the plume had little coalescence, had not glaciated, and were without precipitation, whereas the unpolluted clouds in boxes 1 and 3, side-wind of box 2, had strong coalescence and were precipitating. That observation is corroborated by the PR, which recorded precipitation echoes in the clouds outside, but not within, the plume. The PR-measured rain intensities exceeded 10 mm hour^{-1}. Another large area of clouds with extremely small r_e existed in the Melbourne area and extended downwind to the northeast (box 4). The r_e increased gradually farther downwind but did not reach the precipitation threshold. Farther downwind and to the east of the plume (box 5) only a few isolated showers had formed in some of the clouds that reached the −9°C isotherm and barely exceeded the 14-μm precipitation threshold.

Clouds over the Sydney area (box 6) also had a much reduced r_e, apparently because of the pollution there. Clouds over the sea some 150 km away from Sydney (box 7) had a much larger r_e, indicative of strong coalescence and precipitation in the apparently pristine marine air. The TMI-based TRMM rainfall algorithm identified those clouds as precipitating.

The vertical cross sections (Fig. 5) of the plumes show no obvious differences in the cloud top heights and horizontal dimensions in and outside the areas of suppressed precipitation. Furthermore, the depression of the TMI-measured T_{85} in the nonprecipitating clouds indicates that lack of cloud water was not the reason for the lack of precipitation from these clouds.

The vertical profile of the precipitation echoes as measured by the PR has a distinct maximum near the 0°C isotherm, between 2 and 2.5 km above sea level (Fig. 4). This maximum is caused by the enhanced radar returns from melting snowflakes, known as the "bright band." The existence of the bright band shows that much of the precipitation was initiated as snow in the upper parts of the clouds. That means that the pollution suppressed the precipitation not only by inhibiting the coalescence of the cloud droplets into raindrops but also by preventing the formation of ice particles and cold-precipitation processes of the clouds. A likely explanation is that the pollution reduces the radius of the largest cloud droplets below the threshold of 12 μm, which is required for both primary

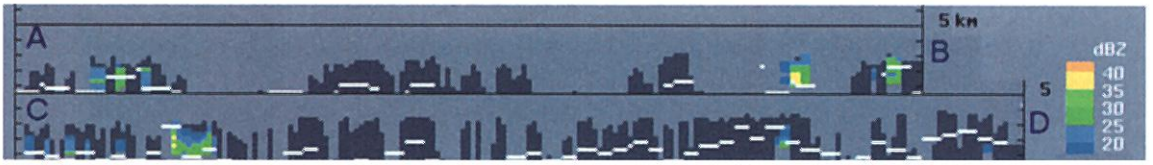

Fig. 5. Vertical cross section along the lines AB and CD in Fig. 2. The dark gray areas represent clouds. The vertical extent of the clouds is converted from the VIRS-measured cloud-top temperatures. The colors represent the precipitation reflectivity in dBZ as measured by the TRMM radar. The white line is the brightness temperature of the TMI 85-GHz vertical polarization (T_{85}), plotted at the altitude of that temperature. A lower T_{85} value is represented as greater height of the white line, and in nonprecipitating clouds it means greater cloud water content. The T_{85} and actual cloud-top temperature have different physical meanings.

and secondary ice generation in clouds (*23*, *24*). Air pollution must be an important factor in determining the precipitation amounts in the Snowy Mountains (east of box 4 in Fig. 2) because it has been observed that most of the winter precipitation events in that region come from clouds with temperature at the tops between −4° and −13°C (*25*). Interestingly, a decreasing trend of the snow cover in the Snowy Mountains was reported for the period 1897–1991 (*25*). However, trend analyses of snow, winter temperature, and total winter rainfall for the period 1910–91 showed statistically insignificant decreases in all three parameters (*26*).

The satellite data provide evidence connecting urban and industrial air pollution to the reduction of precipitation, pinpointing both the sources and the affected clouds. This has become possible with the newly acquired capabilities to observe both cloud microstructure and precipitation over large areas with TRMM satellite observations. It might seem strange that some of the most prominent pollution signatures occur in Australia, which is probably the least polluted inhabited continent. The pollution is perhaps most evident in Australia because it is seen against a background of pristine clouds, whereas in most other places the clouds are already polluted on a very large scale. Such results might indicate that human activity may be altering clouds and natural precipitation on a global scale.

References and Notes

1. P. V. Hobbs and L. F. Radke, *Science* **163**, 279 (1969).
2. Y. J. Kaufman and R. S. Fraser, *Science* **277**, 1636 (1997).
3. P. Squires, *Tellus* **10**, 256 (1958).
4. P. R. Jonas and B. J. Mason, *Q. J. R. Meteorol. Soc.* **100**, 286 (1974).
5. J. Warner, *J. Appl. Meteorol.* **7**, 247 (1968).
6. D. Rosenfeld and I. Lensky, *Bull. Am. Meteorol. Soc.* **79**, 2457 (1998).
7. TRMM was launched on 28 November 1997 as a cooperative project of the National Aeronautics and Space and Administration (NASA) and the National Space Development Agency of Japan (NASDA). The TRMM data are available at http://daac.gsfc.nasa.gov/CAMPAIGN_DOCS/hydrology/hd_trmm_intro.html.
8. D. Rosenfeld, *Geophys. Res. Lett.* **26**, 3105 (1999).
9. R. Gunn and B. B. Phillips, *J. Meteorol.* **14**, 272 (1957).
10. R. C. Eagen, P. V. Hobbs, L. F. Radke, *J. Appl. Meteorol.* **13**, 535 (1974).
11. R. R. Braham Jr., *Meteorol. Monogr.* **18**, 141 (1981).
12. D. B. Johnson, *J. Atmos. Sci.* **39**, 448 (1982).
13. D. F. Gatz, *J. Appl. Meteorol.* **18**, 1245 (1979).
14. E. Jauregui and E. Romales, *Atmos. Environ.* **30**, 3383 (1996).
15. R. S. Cerveny and R. C. Balling Jr., *Nature* **394**, 561 (1998).
16. J. A. Coakley Jr., R. L. Bernstein, P. A. Durkee, *Science* **237**, 1020 (1987).
17. L. F. Radke, J. A. Coakley Jr., M. D. King, *Science* **246**, 1146 (1989).
18. B. A. Albrecht, *Science* **245**, 1227 (1989).
19. Emission data obtained from Flinders Power, Port Augusta, South Australia, Australia.
20. D. Rosenfeld and G. Gutman, *J. Atmos. Res.* **34**, 259 (1994).
21. Information about the TRMM ground validation program is available at http://trmm.gsfc.nasa.gov/trmm_office/field_campaigns/field_campaigns.html.
22. R. Oki *et al.*, *Mar. Technol. Soc. J.* **32**, 13 (1999).
23. S. C. Mossop and J. Hallett, *Science* **186**, 632 (1974).
24. A. Rangno and P. V. Hobbs, *Q. J. R. Meteorol. Soc.* **120**, 573 (1994).
25. B. Harasymiw and J. McGee, *Snowy Precipitation Enhancement Project: A Proposal to Evaluate Feasibility of Increasing Snow Precipitation over the Snowy Mountains Area* (Snowy Mountains Hydroelectric Authority, Cooma, Australia 1993), appendix B.
26. A. L. Duus, *Aust. Meteorol. Mag.* **40**, 195 (1992).

27. I thank all the members of the TRMM team, too numerous to mention individually, for all their hard work to make the satellite a reality and the data of such high quality. The NOAA AVHRR data were obtained from the NOAA Satellite Active Archive. I also thank A. Gingis of Australian Management Consolidated Pty., Ltd. for assisting in this study and W. L. Woodley for help with the manuscript.

5 November 1999; accepted 10 January 2000

An Archaeal Iron-Oxidizing Extreme Acidophile Important in Acid Mine Drainage

Katrina J. Edwards,[1,2]* Philip L. Bond,[1] Thomas M. Gihring,[1] Jillian F. Banfield[1]

A new species of Archaea grows at pH ~0.5 and ~40°C in slime streamers and attached to pyrite surfaces at a sulfide ore body, Iron Mountain, California. This iron-oxidizing Archaeon is capable of growth at pH 0. This species represents a dominant prokaryote in the environment studied (slimes and sediments) and constituted up to 85% of the microbial community when solution concentrations were high (conductivity of 100 to 160 millisiemens per centimeter). The presence of this and other closely related *Thermoplasmales* suggests that these acidophiles are important contributors to acid mine drainage and may substantially impact iron and sulfur cycles.

The oxidative dissolution of metal sulfide minerals causes the formation of acid mine drainage (AMD) and plays an important role in the geochemical sulfur cycle. Sulfides (primarily pyrite, FeS_2) that are exposed to air and water through geological or mining activities undergo oxidative dissolution and generate sulfuric acid by the reaction $FeS_2 + 14Fe^{3+} + 8H_2O \rightarrow 15Fe^{2+} + 2SO_4^{2-} + 16H^+$ (*1*). Mining and extraction mobilizes ~150 × 10^{12} g of sulfur per year, contributing ~50% to the net river transport of sulfate to the ocean, which is about half of the sulfate input into the ocean (*2*).

Microorganisms accelerate the rate of pyrite dissolution through regeneration of Fe^{3+} (*1*, *3*), the primary pyrite oxidant at low pH (*4*–*6*). At Iron Mountain, an AMD site in northern California, the iron-oxidizing bacterium *Thiobacillus ferrooxidans*, previously thought to be the most important iron-oxidizing species, played a minor role in pyrite oxidation (*7*, *8*). Instead, Archaea constituted a large proportion (>50%) of the prokaryote population at important sites of acid generation during the dry summer and fall months

[1]Department of Geology and Geophysics, University of Wisconsin–Madison, 1215 West Dayton Street, Madison, WI 53706, USA. [2]Woods Hole Oceanographic Institute, Department of Marine Chemistry and Geochemistry, Woods Hole, MA 02543, USA.

*To whom correspondence should be addressed at Woods Hole Oceanographic Institute, Department of Marine Chemistry and Geochemistry, Woods Hole, MA 02543, USA. E-mail: kedwards@whoi.edu